

Temperature Dependence of Phosphorus-Based Flame Inhibition

M. A. MACDONALD, F. C. GOULDIN, and E. M. FISHER*

Sibley School of Mechanical and Aerospace Engineering, Cornell University, Ithaca, NY 14853, USA

An investigation of the inhibition properties of Phosphorus-Containing Compounds (PCCs) in moderately strained (global strain rate of 300 s^{-1}) non-premixed methane- $\text{N}_2/\text{O}_2/\text{Ar}$ flames is presented. The effect of DMMP [dimethyl methylphosphonate, $\text{O}=\text{P}(\text{OCH}_3)_2(\text{CH}_3)$] on relative OH concentration profiles was measured by using quenching-corrected Laser-Induced Fluorescence (LIF) for the first time. LIF measurements indicate a reduction in the total OH present of 23% for a non-premixed methane-air flame doped with 572 ppm of DMMP. As the stoichiometric adiabatic flame temperature is increased via substitution of Ar for N_2 in the oxidizer stream, the measurements show a strong decrease in the magnitude of the OH reduction. Experimental results show reasonable agreement with computational predictions made using a kinetic model that has been proposed for DMMP decomposition and phosphorus-radical chemistry. Analysis of the computational results shows that the reactions involving phosphorus remove H and O atoms from the radical pool, thus weakening the flame. These reactions produce OH directly, but the rest of the mechanism responds to O and H reductions by reducing OH levels. The key reactions involved in this inhibition process are identified. © 2001 by The Combustion Institute

INTRODUCTION

Since the advent of the Montreal Protocol in the 1990, which banned the manufacture of a variety of halogenated compounds including the fire suppressant CF_3Br , there has been a strong interest in the development of new chemically active fire suppressants. One of the classes of compounds that are under consideration are phosphorus-based agents, such as DMMP [dimethyl methylphosphonate, CAS #756-79-6, $\text{O}=\text{P}(\text{OCH}_3)_2(\text{CH}_3)$]. Extinction measurements on non-premixed, atmospheric-pressure flames have demonstrated DMMP to be a highly effective suppressant (2–4 times more effective than CF_3Br) [1]. Even when used in quantities that are insufficient to cause extinction, fire suppressants are generally observed to inhibit flame chemistry via physical and chemical effects. The mechanism for phosphorus-based inhibition is believed to be catalytic recombination of flame radicals (H, OH, O) by phosphorus-containing radicals [2, 3] formed following the decomposition of the parent compound [2, 4]. This mechanism is analogous to that of halogen-based suppressants [5, 6]. The influence of phosphorus-containing compounds (PCCs) on radical concentrations in flames has been demonstrated

experimentally. Chemiluminescent emission spectroscopy was used to observe changes in OH by Ibricic and Gaydon [7] as well as Hastie and Bonnell [2], who also observed changes in H atom concentrations by using a Li/Na emission technique. Qualitative laser-induced fluorescence (LIF) measurements have shown reductions in OH fluorescence because of the addition of DMMP [8]. In addition, quantitative laser absorption measurements of OH in a flow reactor have shown that the addition of PH_3 (phosphine) to $\text{H}_2\text{-O}_2$ combustion product gases increases H + OH recombination rates following laser photolysis [3]. A more complete literature review of the influence of PCCs on flames can be found in [1, 5].

Extinction studies under a variety of flame conditions found a significant temperature dependence for DMMP effectiveness, with higher effectiveness being observed at lower stoichiometric adiabatic flame temperatures [9]. The existence of a temperature dependence for phosphorus-based flame inhibition was first suggested by Hastie and Bonnell in 1980 [2], but since then there has been little investigation of this behavior. There is one computational study on premixed flame speeds [5], but aside from [9] there is no experimental work, of which we are aware, in which flame temperature has been systematically varied. The influence of flame

*Corresponding author. E-mail: emf4@cornell.edu.

TABLE 1

Flame Conditions

Flame #	Oxidizer Composition	$T_{\text{adiabatic}}$ [K]	$T_{\text{calculated peak}}$ [K]	DMMP [ppm]	V_O [cm/s]	V_F [cm/s]
1	21% O ₂ -79% N ₂	2261	1967	0-572	71	96
2	21% O ₂ -53% N ₂ -26% Ar	2353	2080	0-715	71	101
3	21% O ₂ -26% N ₂ -53% Ar	2450	2189	0-715	71	106
4	21% O ₂ -79% Ar	2547	2286	0-715	71	110

temperature on inhibition effectiveness is an important consideration in evaluating the feasibility of new phosphorus-based flame suppressants, and has direct bearing on how to maximize their effectiveness in practical applications. The indicated trend implies that a mixture of inert and phosphorus-based suppressants could interact synergistically as the inert component cools the flame, thus increasing the efficiency of the chemically active component. The use of suppressant mixtures not only increases the overall efficiency of the suppression system, but dramatically lowers the quantity of the chemically active component used, thus decreasing environmental concerns and possible health impacts. A similar temperature dependence has been demonstrated for CF₃Br, including the observation of synergistic interaction with the inert suppressants N₂, CO₂, and H₂O [10, 11]. Increased effectiveness at lower flame temperatures has also been observed for the iron-based suppressant Fe(CO)₅ [12, 13].

Our goals for the current study are to unambiguously identify and quantify the temperature dependence for flame inhibition by DMMP and to gain further insight into the inhibition mechanism. To this end, the influence of DMMP on OH concentration profiles has been studied in an opposed-jet burner using quenching-corrected laser-induced fluorescence (LIF). Only a limited number of measurements of OH concentrations in the counterflow configuration have been reported [14-17]. Several studies have utilized LIF to observe changes in OH concentration in flames doped with halogenated suppressants [18-20], while work with flames doped with phosphorus-containing agents is far more limited [8, 16]. In the present work, the inhibition "effectiveness" of DMMP is evaluated in terms of the reduction in OH concentration due to its presence. A series of four non-premixed, atmospheric-pressure flames of

methane versus O₂/N₂/Ar mixtures were studied. Flame temperature was varied by changing the proportions of N₂ and Ar in the oxidizer side diluent, while maintaining 21% (by vol) O₂ and thus a constant stoichiometric mixture fraction of 0.055. Experimental results are also compared to predictions from numerical calculations made using a kinetic mechanism [16] that has been proposed for DMMP decomposition and phosphorus-containing radical chemistry. The key reactions in the mechanism that are responsible for the observed inhibition of OH are identified.

EXPERIMENTAL METHOD

Measurements

Our opposed-jet burner geometry and dopant delivery system have been detailed previously [1, 9]. The reactant nozzles are straight glass tubes without screens (0.98 cm i.d.) with a separation distance of 0.95 cm between opposing nozzles. Methane fuel flows from the lower tube, and the oxidizer is introduced from the upper tube. Reactant streams are maintained at 100°C, to prevent DMMP from condensing on reactant tube walls. Table 1 lists the composition and stoichiometric adiabatic flame temperatures for the four flames studied; note that these temperatures are slightly higher than typical due to the reactant preheat. All flames have a global strain rate, a , of 300 s⁻¹ as calculated from reactant stream flow rates and nozzle geometry using Eq. 1 [21]:

$$a = \frac{2V_O}{L} \left(1 + \frac{V_F}{V_O} \left(\frac{\rho_F}{\rho_O} \right)^{1/2} \right). \quad (1)$$

L refers to the separation distance between the nozzles; V is the volume averaged stream veloc-

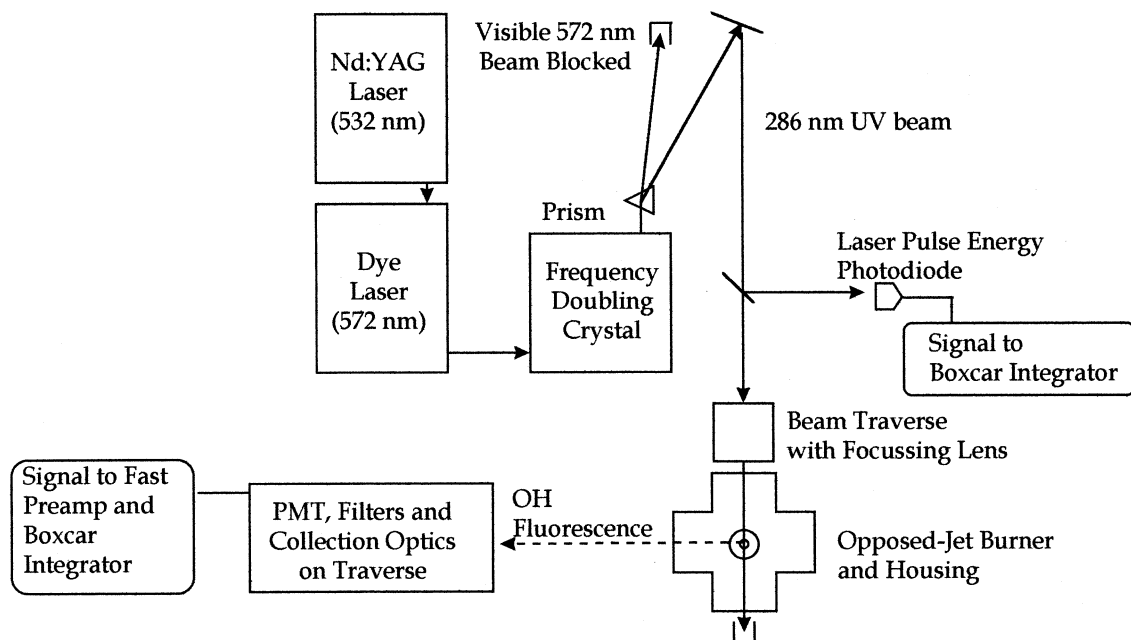


Fig. 1. Schematic of LIF apparatus.

ity; and ρ is the stream density, with the subscripts O and F referring to oxidizer and fuel respectively. Equation 1 assumes plug flow boundary conditions at the nozzle exit planes. The fuel and oxidizer velocities are chosen to be momentum balanced, which places the stagnation plane in the center of the burner in the absence of a flame. When the flame is established, these conditions lead to a stable, laminar flame that is well centered in the burner.

Calculations of the undoped flames were made using the OPPDIF code version 8.5 from the CHEMKIN III Suite [22]. The full GRI-MECH 3.0 mechanism, including nitrogen chemistry, (53 species, 325 reactions) [23] was employed. Mixture averaged diffusion velocities were used, and thermal diffusion was neglected. Opposed-jet burners are typically modeled as having either potential flow (linear axial velocity gradient) or plug flow (zero axial velocity gradient) boundary conditions, although measurements indicate that the actual velocity field lies somewhere between the two approximations [24]. Calculations were performed for several different boundary conditions, as described below. The boundary conditions of potential flow with centerline axial velocities of twice the measured volume averaged velocities for the

fuel and oxidizer streams were selected for use in this study, because the resulting OH profiles most closely agreed with our observed profiles. The factor of two for the centerline velocities is appropriate because the flow in the straight-tube reactant nozzles ($L/D > 30$) is expected to be close to Poiseuille flow, in which the centerline velocity is twice the volume average. Temperature profiles predicted by 1D calculations have been found by other researchers to be in good agreement with measurements made in opposed-jet burners under a variety of conditions by using spontaneous Raman scattering in $\text{CH}_4/\text{O}_2/\text{N}_2$ [25] and H_2/air [14] flames, thin SiC filament pyrometry in $\text{CH}_4/\text{O}_2/\text{N}_2$ flames [26] and CARS in propane/air flames [27].

OH concentration measurements were made by using point-wise LIF. Figure 1 shows a schematic of the experimental set up. Profile measurements were made by traversing the laser beam and collection optics simultaneously across the flame in $100 \mu\text{m}$ steps. The translation stages used have a resolution of $10 \mu\text{m}$. Excitation of the $P_1(9)$ transition of the $A \leftarrow X(1, 0)$ band near 286 nm was made by using a frequency-doubled Quanta Ray PDL 2 pulsed dye laser, nominal linewidth of 0.2 cm^{-1} , with rhodamine 590 dye. This transition was selected

because of the weak temperature dependence of the rotational ground state population in the temperature region of interest ($<10\%$ variation for $1400\text{ K} < T < 2500\text{ K}$), which helps maintain a strong LIF signal across the entire OH profile. The dye laser was pumped with a 6 to 7 ns pulse at 532 nm provided by a frequency-doubled Spectra Physics DCR 2A Nd:YAG laser operating at 10 Hz.

Detection of OH fluorescence was performed at 90° to the laser beam axis using an RCA 8850 photomultiplier tube and color glass filters (Schott WG305 and UG11) which transmit light in the 305 to 371 nm range. The photomultiplier signal was amplified by a SRS240 Fast Preamplifier (Stanford Research Systems). The filter combination used blocks elastically scattered laser light (and near-elastic resonant fluorescence) while passing fluorescence emission from the (1, 1) band (312–326 nm) and emission from the overlapping (0, 0) band (306–320 nm) which can occur following collisionally driven Vibrational Energy Transfer (VET) from the $\nu' = 1$ to the $\nu' = 0$ states. At atmospheric pressure, VET rates can be significant [28, 29] with more than a third of the total measured fluorescence originating from the (0, 0) band when using excitation/detection schemes similar to ours [30]. Fluorescence trapping of emission from the (1, 1) band is negligible because of the small population of the electronic ground state with $\nu' = 1$ over the temperature range under consideration. Some trapping will occur for fluorescence emission originating from the (0, 0) band, but the effect is small due to the short path length through the flame (less than 1 cm) and is not expected to influence the measurements [31, 32]. PAH fluorescence is a common form of interference observed when using this excitation/detection scheme, if significant levels of PAH are present [31]. The moderately strained laminar flames under investigation here are virtually soot-free, and consequently PAH fluorescence was expected to be low. Measurements taken with the dye laser tuned off resonance confirmed that interference from PAH was negligible. The combination of the focussed ($f = 30\text{ cm}$ quartz focussing lens) UV laser beam and slits in the detection optics give a probe volume of less than $100\ \mu\text{m}$ in diameter and 1.5 mm in length. The opposed-jet burner

flame is locally planar near the centerline with the long axis of the probe volume aligned in the plane of the flame surface. Laser pulse energy was monitored using a UV-sensitive photodiode. Both the LIF and laser energy signals were integrated on a shot-by-shot basis using an SRS 250 Boxcar Integrator and Averager (Stanford Research Systems), and recorded on a personal computer using a GW Instruments data acquisition card. Operation within the linear LIF regime was ensured by checking the linearity of LIF signal strengths with pulse energy for all measured data points [33].

To avoid errors associated with wavelength drift of the dye laser and the resulting changes in the spectral overlap of the laser and molecular absorption lineshapes, the output wavelength of the dye laser was scanned across the $P_1(9)$ transition at each measurement location using a stepper motor to adjust the grating in the dye laser cavity. 100 measurements of OH fluorescence and laser pulse energy were acquired at each half-step of the motor (one half-step corresponds to a wavelength change of approximately 0.0012 nm), and the half-step motor position with the maximum average ratio of fluorescence signal to laser pulse energy was taken to be the absorption line center for the transition. LIF data for that half-step motor position were used for the subsequent evaluation of OH concentration. The repeatability of this procedure was found to be within $\pm 5\%$ of the mean observed ratio. The average ratio of OH fluorescence signal to laser pulse energy was found by fitting the 100 measurements to a straight line by linear regression analysis. The statistical uncertainty (one standard deviation) in the fitted slopes was less than $\pm 3\%$. Additional uncertainty in these slopes arises from statistical uncertainty in the measurement of the zero level in the presence of electrical noise from the Nd:YAG laser. Statistical scatter in the zero measurement (\pm one SD) corresponds to an uncertainty of ± 3 to 5% of the peak slope for all data points in the profile. In addition to shot noise and electrical noise, the statistical uncertainty in the measurements reflects fluctuations in flame location. For these aerodynamically stabilized flames, perturbations in the reactant flow can cause small, momentary flame displacements. The 100 shot LIF averaging process

will largely compensate for these oscillations if they occur. Particularly for measurements made in regions where the curvature of the OH profile is not large, that is, away from the immediate vicinity of the OH peak and the profile edges, small, random fluctuations in flame position yield symmetric fluctuations in the LIF signal that will average to zero. The total uncertainty for each measured data point in a given profile due to these random errors was found by summing the contribution of the uncertainties described above (assuming statistical independence) and is estimated to be less than $\pm 10\%$ of the peak value in the profile. Uncertainty estimates will be illustrated for sample profiles in the Results section.

To quantify the fluorescence measurements, corrections for collisional quenching and the fraction of the OH population that is in the pumped rotational level must be made. However, the overall effect of these corrections on the profile shape is small, as is expected for our excitation/detection scheme in non-premixed atmospheric-pressure flames [17, 34, 35]. Equation 2 relates the fluorescence signal to the concentration of OH assuming low laser energy (i.e., negligible saturation of the excited transition) [36]:

$$F = CBI f N \Phi. \quad (2)$$

Here F is the total fluorescence signal; C is a constant that incorporates geometric factors such as collection solid angle and probe volume as well as detector efficiencies and gain characteristics of the integrators, amplifiers etc.; B is the Einstein coefficient for stimulated absorption; I is the spectral overlap integral between the laser intensity and the molecular absorption lineshape, temporally integrated over the duration of the laser pulse; N is the total OH population, and f is the fraction of the population that is present in the ground state rotational level excited by the laser; and Φ is the fluorescence quantum yield, which depends on the local quenching and VET rates.

Species and temperature profiles from the undoped-flame calculations were used to estimate the required corrections to the linear LIF data for both doped and undoped flames. The fraction of the ground state population in the pumped rotational level is determined using the local gas temperature given by the calculations

and assuming rotational thermal equilibrium (Boltzmann distribution), as implemented in the spectral simulation software LIFBASE [37].

The total fluorescence yield can be estimated by using [30]:

$$\Phi = \frac{A_1 + \frac{V_{10}}{Q_0} A_0}{Q_1 + V_{10}}, \quad (3)$$

where A_1 and A_0 are the spontaneous emission rates for the $\nu' = 1$ and $\nu' = 0$ vibrational levels, respectively. Equation 3 has been simplified by assuming equal transmission and detection efficiencies of the collection optics and PMT for both the (1, 1) and (0, 0) bands. Q_1 and Q_0 are the total quenching rates for the $\nu' = 1$ and $\nu' = 0$ levels, and V_{10} is the total VET rate from $\nu' = 1$ to $\nu' = 0$. The influence of VET rates on the fluorescence quantum yield is primarily because of the higher spontaneous emission rate of the $\nu' = 0$ state ($A_1/A_0 \approx 0.575$) [38]. The quenching and VET rates are evaluated using Eq. 4 [30, 38]:

$$Q, V = (P/(k_b T)) \sum_i \chi_i \langle \nu \rangle_{i-\text{OH}} \sigma_i^{Q,V}(T), \quad (4)$$

where P is pressure; T is temperature; k_b is Boltzmann's constant; χ_i is the mole fraction of OH collision partner species i ; $\langle \nu \rangle_{i-\text{OH}}$ is the mean relative collision velocity of species i and OH given by $\langle \nu \rangle_{i-\text{OH}} = (8k_b T / \pi \mu_{i-\text{OH}})^{1/2}$, where $\mu_{i-\text{OH}}$ is the reduced mass of species i and OH; and $\sigma_i^{Q,V}(T)$ is the value of the quenching or VET (superscript Q or V , respectively) cross section for collisions with species i , averaged over all rotational levels in a given vibrational level, assuming rotational thermal equilibrium.

Substitution of Eq. 4 into Eq. 3 followed by some algebraic manipulation yields [30]:

$$\Phi = \frac{A_0}{Q_0} \left[\frac{\left(\frac{A_1}{A_0}\right) \left(\frac{\langle \sigma^Q \rangle_0}{\langle \sigma^Q \rangle_1}\right) + \frac{\langle \sigma^V \rangle_{10}}{\langle \sigma^Q \rangle_0}}{1 + \frac{\langle \sigma^V \rangle_{10}}{\langle \sigma^Q \rangle_1}} \right], \quad (5)$$

where $\langle \sigma^Q \rangle_1$, $\langle \sigma^Q \rangle_0$, and $\langle \sigma^V \rangle_{10}$ represent the sum over all collision partners of the thermally averaged cross sections for quenching from $\nu' = 1$, quenching from $\nu' = 0$, and VET from $\nu' = 1$ to $\nu' = 0$, respectively. Fewer quenching cross-section measurements have been made

for the $\nu' = 1$ state than for $\nu' = 0$ [28, 39], but results indicate similar values to those found for the $\nu' = 0$ state. We have therefore approximated the quenching environment for both states as being that for the $\nu' = 0$ state, or equivalently $\langle\sigma^Q\rangle_1/\langle\sigma^Q\rangle_0 \approx 1$. The ratio of averaged VET cross sections to the averaged quenching cross sections is assumed to be independent of position in the flame (e.g., $\langle\sigma^V\rangle_{10}/\langle\sigma^Q\rangle_0 \approx \text{constant}$). As a result, the quantity in square brackets in Eq. 5 becomes a constant, and the fluorescence yield is simply inversely proportional to the quenching rate for the $\nu' = 0$ state (taken to be equal to that for $\nu' = 1$). To confirm the validity of the assumption $\langle\sigma^V\rangle_{10}/\langle\sigma^Q\rangle_0 \approx \text{constant}$, we have estimated the VET rates and resulting fluorescence yield according to Eqs. 3 and 4, by using the limited available VET cross-section data [28, 39, 40], some of which are reported only as upper bounds, along with major species and temperature profiles from calculations. These estimates indicate that the error in the fluorescence quantum yield introduced by this approximation is less than 5%. Values for the quenching rate cross-sections used in this work are taken from temperature-dependent quenching cross-section data compiled by Tamura et al. [41] from the extensive measurements that have been made for the $\nu' = 0$ state of OH.

The calculated quenching rate varies by 15% across the OH containing regions in flame 1. This variation is moderated by the presence of a large concentration of N_2 which has a relatively small gradient in the flame zone. For flame 4, where Ar (a highly inefficient quencher) has been substituted for N_2 , the variation is substantially higher at 30%.

The same quenching environment was assumed for flames both with and without DMMP loading. The maximum phosphorus loading was only 715 ppm. Because the mole fractions of phosphorus-containing species will be small in this case, it is expected that they will not contribute significantly to quenching of OH. Changes in major species profiles because of the presence of DMMP are not expected to be large enough to significantly change the overall quenching environment. Changes in flame temperature due to the addition of these small loadings of DMMP (see Calculations with Phos-

phorus Kinetics section) were also found to be negligible (<10 K).

After correcting for the fluorescence yield and the Boltzmann fraction of the pumped rotational level, the corrected LIF profile is directly proportional to OH concentration. An estimate of the scaling constant relating the corrected LIF measurements to absolute OH concentrations can be made by matching the peak of the measured profile from the undoped flame to the peak OH concentration predicted by the flame calculations. This matching does not affect our observations of PCC effects on OH, which are all presented normalized to the undoped flame measurements. For profiles measured in flames doped with phosphorus-containing additives, the scaling constant is determined from undoped profiles taken on the same day with the same instrument settings. Because the same constant is used for both doped and undoped flames, quantitative comparisons can be made between the two cases. Determination of the magnitude of the scaling constant is performed by minimizing the mean-square-error between calculated and measured profiles (via a least squares technique). For this minimization, only data points above 50% of the measured peak value were considered. Minimization of error was performed via adjustment of the scaling constant and a position offset (i.e., the offset between the measured flame center, as indicated by the translation stage micrometers, and the computational flame center). Determination of this scaling constant essentially calibrates the constant C from Eq. 2, assumed to be constant for a given set of instrument settings. This scaling procedure affects only the magnitude and position of the observed fluorescence profile and not the shape or width.

Calculations with Phosphorus Kinetics

To investigate the cause of the OH concentration changes observed in the LIF experiments, a set of flame calculations was performed using a proposed mechanism for DMMP decomposition and phosphorus-radical chemistry [16] that has been developed in recent years. This mechanism is based on 1) the kinetic data used for the analysis of the influence of PH_3 on radical

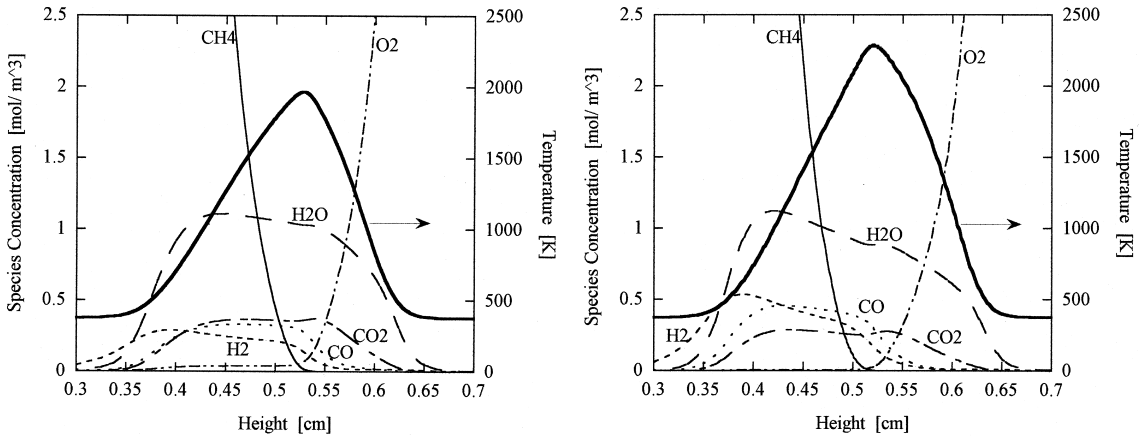


Fig. 2. a) Calculated major species and temperature profiles for Flame 1, undoped. b) Calculated major species and temperature profiles for Flame 4, undoped.

recombination rates in the combustion products of a hydrogen flame [42, 43] and 2) kinetic models used for describing DMMP and TMP [trimethyl phosphate, CAS#512-56-1, $P(=O)(OCH_3)_3$] destruction in a low pressure hydrogen flame [44, 45]. Reactions of phosphorus-containing species with radicals and intermediate species of hydrocarbon combustion have been included [16]. Reactions have been added to the scheme to complete destruction pathways for some species [16]. The current version of this phosphorus mechanism includes 27 species and 166 reactions. Thermochemical data compiled by Babushok [46] for phosphorus-containing species are mostly taken from Refs. [3, 47–49]. Methane- O_2 chemistry was modeled using GRI Mech 3.0 [23] with nitrogen chemistry removed (36 species, 219 reactions retained). The phosphorus mechanism predicts reductions in extinction stain rates for non-premixed methane-air flames because of the presence of DMMP [16] that are in agreement with experimental results from MacDonald et al. [1]. An earlier version of the mechanism has also been used to predict the effect of DMMP on premixed flame speeds [5]. Figures 2a and 2b illustrate the major species profiles from these calculations for flames 1 and 4 without dopant addition. Calculations were performed for all four flames using the combined mechanisms (phosphorus and GRI Mech), both with and without the addition of 572 ppm of DMMP. Calculations with the combined mechanisms required a higher degree of mesh refinement (both GRAD and CURV parameters for OPP-

DIF script = 0.1, yielding 250–300 grid points) than the GRI Mech calculations to produce OH profiles for the doped flames that were independent of grid size.

RESULTS

Measurements

Figure 3 shows a comparison between measured and calculated OH concentration profiles for flames 1 and 4, the coolest and hottest conditions respectively. Multiple profiles, all un-

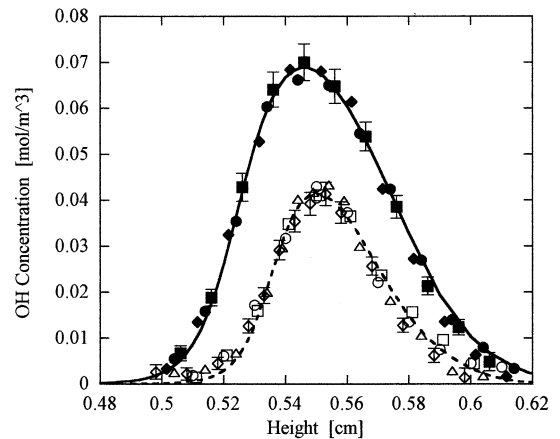


Fig. 3. OH concentration profiles. Flame 1 computations are shown as the dashed line; open symbols are for four measured profiles. Flame 4 computations are shown as the solid line; filled symbols are for three measured profiles. Error bars represent statistical uncertainty in the measured values.

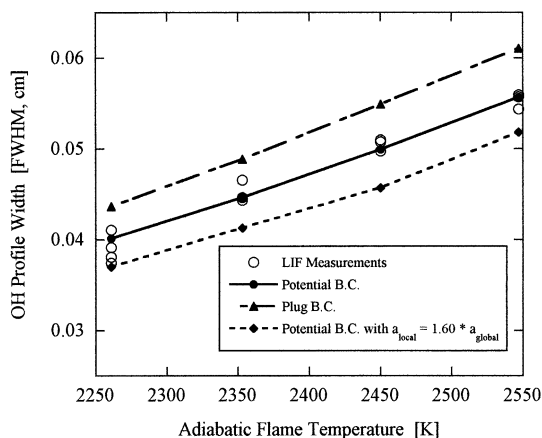


Fig. 4. OH profile widths (FWHM). Open circles are measured values for all undoped flames. Lines with filled symbols are computational values for three different velocity boundary conditions (B.C.). Filled circles are potential flow B.C. with velocities of twice the volume average (Poiseuille flow). Filled triangles are plug flow B.C. with velocities equal to the volume average. Filled diamonds are potential flow B.C. with local strain rate equal to 1.60 times the global strain rate given by Eq. 1.

doped, are shown to illustrate the repeatability of these measurements. The agreement between measured and calculated profiles is seen to be quite good. The intermediate cases of flames 2 and 3 are in similar agreement between measured and computed profiles. Agreement in peak OH concentration is expected since calculated profiles are used to estimate peak concentrations in our measurements for each flame. There is also good agreement in the profile shape, which is not affected by the matching procedure, including the degree of asymmetry, and width (FWHM). The peak concentration, as determined by the calculations, is seen to increase by 66% from 0.041 mol/m^3 for flame 1 to 0.069 mol/m^3 for flame 4, which has a stoichiometric adiabatic flame temperature that is 286 K hotter than flame 1. It should be noted that the peak temperatures, from laminar flame calculations (see Table 1), for these moderately strained flames are approximately 300 K cooler than the stoichiometric adiabatic flame temperatures, although the difference in calculated peak temperatures for flames 1 and 4 (319 K) is comparable to the change in the stoichiometric adiabatic flame temperature (286 K).

Figure 4 illustrates the variation in computed and measured OH profile widths (FWHM) with

adiabatic flame temperature. All flame conditions are undoped. Both the calculated and measured OH profile widths are observed to increase by approximately 40%, from 0.4 mm to 0.55 mm, across the range of temperatures investigated. Good agreement between calculated and measured profile widths is observed for all undoped flames.

The velocity boundary conditions in the calculations can also have a noticeable effect on the calculated width of the OH profile. To investigate the influence of these boundary conditions, two additional sets of calculations were performed, one for plug flow boundary conditions with the measured volume averaged velocities and the other for potential flow while matching the maximum local strain rate to 480 s^{-1} , or 1.60 times the global strain rate (Eq. 1) (which required increasing the centerline velocity for the calculations to 2.8 times the volume averaged value). The higher strain case was motivated by measurements of axial velocity profiles made using Laser-Doppler Velocimetry (LDV) in a similar burner configuration [50]. These measurements indicated a substantially higher local strain rate (axial velocity gradient on the oxidizer side, evaluated just upstream of the heat release region) of approximately 1.60 times the global strain rate. The original calculations, with boundary conditions of potential flow and velocities of twice the volume average, gave a computed velocity profile with a peak local strain rate of approximately 1.18 times the global strain rate or 355 s^{-1} . The calculated OH profile widths for the two additional sets of boundary conditions are also shown in Fig. 4. Both additional sets of boundary conditions predict similar variation in profile width with flame temperature. However, the plug flow boundary condition overestimates the profile widths by 10 to 15%, and the higher strain rate case underestimates the widths by 5 to 8%. Finite spatial resolution in the measurements ($100 \mu\text{m}$) limits the accuracy with which the experimental width can be determined. Heat and radical losses to the burner as well as radiation, which are ignored in those calculations, will also contribute to the discrepancy between measured and calculated profiles. However, these physical loss mechanisms are not expected to be significant in these well

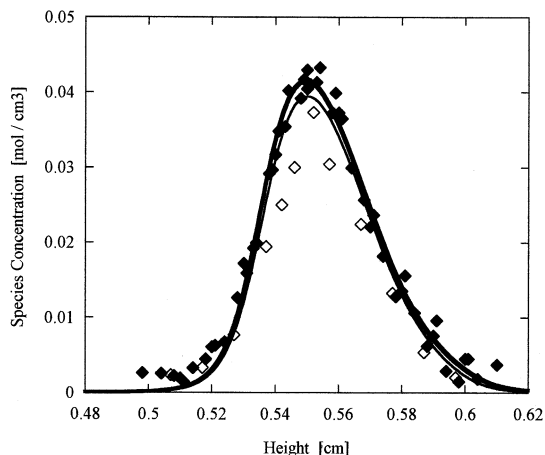


Fig. 5. Effect of 572 ppm of DMMP on OH in Flame 1. Filled symbols are for undoped profiles; open symbols are for doped profile. The thick line shows the computational prediction for the undoped profile; thin line is the doped profile. Phosphorus kinetic mechanism from Wainner et al. [16].

isolated, non-sooting flames. Uncertainties associated with the chemical mechanism used will influence the computed profile width and also affect the level of agreement between computed and measured profile widths.

The good agreement between the measured profiles and the calculations made with potential flow boundary conditions with centerline velocities of twice the volume average support our selection of this boundary condition for use in the quenching and Boltzmann fraction corrections to the LIF data. It should be noted that because of the relatively small impact of the temperature and quenching correction, the choice of the appropriate boundary conditions does not substantially influence the conclusions below about the influence of phosphorus additives on OH concentration. Using profiles calculated with either of the alternate boundary conditions to correct the LIF data changes the observed reductions in total OH by less than 1%, well within the uncertainty of the measurements.

Figure 5 illustrates the effect of 572 ppm of DMMP on OH concentrations in flame 1. With this loading, flame 1 is close to extinction. A substantial reduction, approximately 20%, in OH concentration is observed. The doped profile is seen to be smaller in magnitude, but the width is not significantly affected. To determine

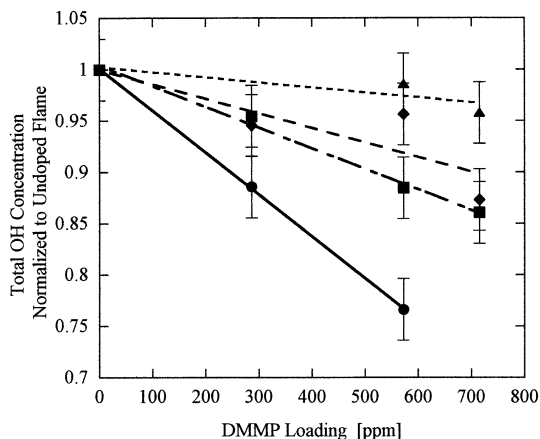


Fig. 6. Effect of DMMP loading for all flames. Lines are linear regression fits to data. Solid line and circles are Flame 1, dot-dash line and squares are Flame 2, dashed line and diamonds are Flame 3, dotted line and triangles are Flame 4. Error bars represent uncertainty in measurements.

changes in the total flame OH concentration, the profiles are numerically integrated, using a simple trapezoidal rule approximation, across the width of the flame, and then the integrals from the doped and undoped flames are compared. The integration technique is particularly useful for quantifying changes in the higher-temperature flames where the OH concentration profile is less affected by the phosphorus-containing additive. There is a $23 \pm 3\%$ reduction in total OH (by this definition) for the data shown in Fig. 5. The uncertainty results from the estimated statistical uncertainty of the individual data points from the profile, and is closely comparable to the repeatability of the measurement.

OH concentration profiles were measured for all four flames with DMMP loadings up to 715 ppm, with the exception of flame 1. A loading of 715 ppm of DMMP in flame 1 is sufficient to cause extinction, at the global strain rate used in this study. Therefore, the maximum loading used for that flame was 572 ppm, the next highest loading readily achieved experimentally. Figure 6 illustrates the ratio of doped to undoped total OH for the four flames as a function of loading. Raw data for profiles for all conditions studied in this work can be found in the appendix of Ref. [51]. Total OH appears within experimental uncertainty to decrease linearly with DMMP addition over this range of load-

ings. Results from the calculations performed with the phosphorus kinetic mechanism, discussed below, for a range of DMMP loadings from 0 to 720 ppm, confirmed the linear variation in the OH reduction with loading. The linear trends are consistent with extinction measurements on non-premixed methane-air flames which indicated a linear variation in DMMP effectiveness, defined in terms of reduction in the global extinction strain rate, for loadings up to 1500 ppm [1]. Linear variation in effectiveness with loading is observed with most flame suppressants at low loadings. Linear regression fits to the data for each flame are also shown in Fig. 6. The most striking observation from Fig. 6 is the increase in inhibition effectiveness with decreasing flame temperature. The highest-temperature case, flame 4, shows less than 5% reduction in total OH at the maximum loading of 715 ppm, compared to 23% reduction in flame 1 for only 572 ppm.

We attempted extinction measurements for the flames in this work, but were not successful because the high extinction strain rates for flames 2 through 4 required dramatically higher flow velocities that were well into the turbulent flow regime for our geometry. However, in an earlier study we investigated the effect of DMMP on global extinction strain rate for a variety of different flame conditions with different stoichiometric mixture fractions and stoichiometric adiabatic flame temperatures [9]. Effectiveness in terms of extinction strain rates for that work was defined as the fractional reduction in global extinction strain rate divided by the mole fraction of phosphorus in the flame:

$$\text{Effectiveness}_q \equiv \frac{(a_{q,0} - a_q)}{a_{q,0}} \frac{1}{\chi_P}. \quad (6)$$

The subscript q indicates that the measurement is made at extinction conditions, and the subscript 0 denotes the value for the undoped flame. Flame calculations were used to estimate the mole fraction of phosphorus at the flame surface, χ_P , taken to be the maximum temperature contour. We observed a similar trend of decreasing effectiveness with increasing temperature. The stoichiometric adiabatic flame temperature in that study was varied in two ways. The first was by changing the stoichiometric

mixture fraction from 0.05 to 0.7 while maintaining a fixed undoped global extinction strain rate. The second was by decreasing the overall dilution of the flame while maintaining a stoichiometric mixture fraction of 0.5. The range in adiabatic flame temperatures from that work (2130–2260 K) is substantially lower than that investigated here. To compare the temperature dependence from the previous investigation to that of the current work, we define a measure of effectiveness, analogous to the one used in the previous study, in terms of OH reduction as the fractional reduction in total OH concentration:

$$\text{Effectiveness}_{\text{OH}} \equiv \frac{(\text{TotalOH}_0 - \text{TotalOH})}{\text{TotalOH}_0} \frac{1}{\chi_P}. \quad (7)$$

Again, the subscript 0 denotes the measured value for the undoped flame. The flame calculations made with the combined GRI Mech and phosphorus mechanisms are used to determine χ_P , the total mole fraction of phosphorus (sum of mole fractions of all phosphorus-containing species) predicted at the flame surface, taken to be the maximum temperature contour. Because the stoichiometric mixture fraction is fixed for all flames, changes in χ_P are negligible. The use of this parameter in the current work does not affect the observed trends and is introduced solely to provide a definition for effectiveness that is analogous to that used in Ref. [9] to facilitate a comparison to our previous extinction studies. This effectiveness definition is essentially a measure of the slope of the linear trends indicated in Fig. 6. Figure 7 shows a comparison of this effectiveness based on OH with the one based on the extinction measurements from the previous study. The trends observed in the two data sets are in good qualitative agreement, given that different measures of effectiveness are used. When comparing the two data sets, it should also be noted that for a given stoichiometric adiabatic flame temperature, measurements performed at extinction conditions, such as those from [9], will have a peak flame temperature that is cooler than that seen in the LIF measurements, which are performed at a fixed global strain rate of 300 s^{-1} , below the value required to extinguish the flame. The effectiveness data in Fig. 7 shows a

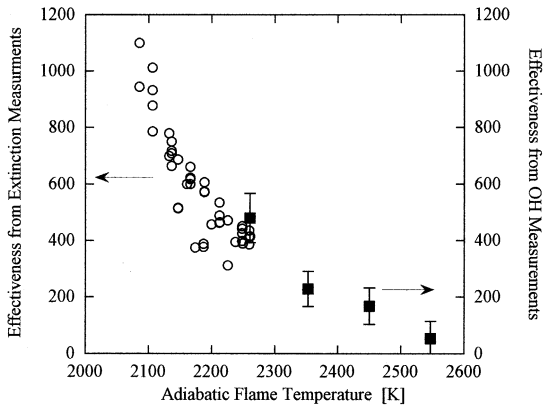


Fig. 7. Temperature dependence of effectiveness. Open circles are effectiveness data from Ref. [9] defined in terms of reduction of global extinction strain (Eq. 6). Filled squares are effectiveness data from the current work defined in terms of reduction in OH concentration (Eq. 7). Error bars represent uncertainty in the measurements.

substantial decrease in DMMP effectiveness with increasing temperature. The unambiguous trends in the LIF data confirm the hypothesis of Hastie and Bonnell [2] of decreasing inhibition with increasing flame temperature, with nearly a 90% decrease in effectiveness for a 300 K increase in temperature.

Calculations with Phosphorus Kinetics

The combined mechanism of phosphorus kinetics by Wainner et al. [16] and $\text{CH}_4\text{-O}_2$ kinetics from GRI Mech [23] was used to calculate species and temperature profiles for all four flames with and without the addition of 572 ppm of DMMP. The predicted temperature profiles showed no significant effect from the addition of DMMP (<10 K change in peak temperature). However, significant changes were observed in OH, H, and O profiles. Figure 8 illustrates the doped and undoped profiles of OH, H, and O for flame 1. Relative to the undoped profile, the OH profile for the doped flame is lower in magnitude. The change is similar to that observed in the measured data, but not as large. A comparison of computational predictions to measured data is shown in Fig. 5. It is interesting that the reduction in H and O atom concentrations seen in Fig. 8 is significantly greater than the reduction for OH, indicating a larger effect of phosphorus chemistry on the concentrations of those species.

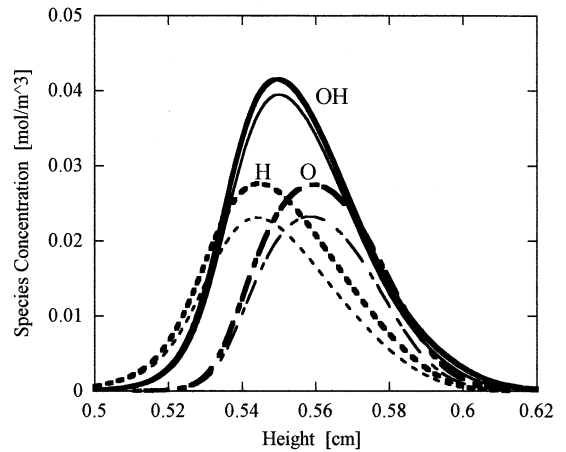


Fig. 8. Effect of 572 ppm of DMMP on calculated OH, H, and O concentration profiles in Flame 1 ($\text{CH}_4/\text{O}_2/\text{N}_2$). Dark lines are undoped profiles and thin lines are with DMMP addition.

After performing the spatial integration of the computed profile across the flame, as described above, the change in total OH between the doped and undoped cases is evaluated. Figure 9 shows a plot of effectiveness, as defined in terms of OH reduction (Eq. 7), as a function of the stoichiometric adiabatic flame temperature for both the experiments and the computations. The computational and experimental results in Fig. 9 display the same trend of decreasing effectiveness with increasing temperature, al-

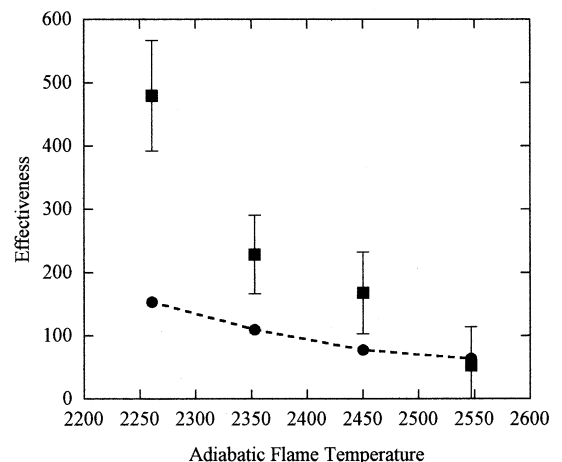


Fig. 9. Temperature dependence of effectiveness defined as in terms of reduction in total OH (Eq. 7). Filled circles with the dashed line are computational predictions, filled squares are measured data. Error bars represent uncertainty in the measurements.

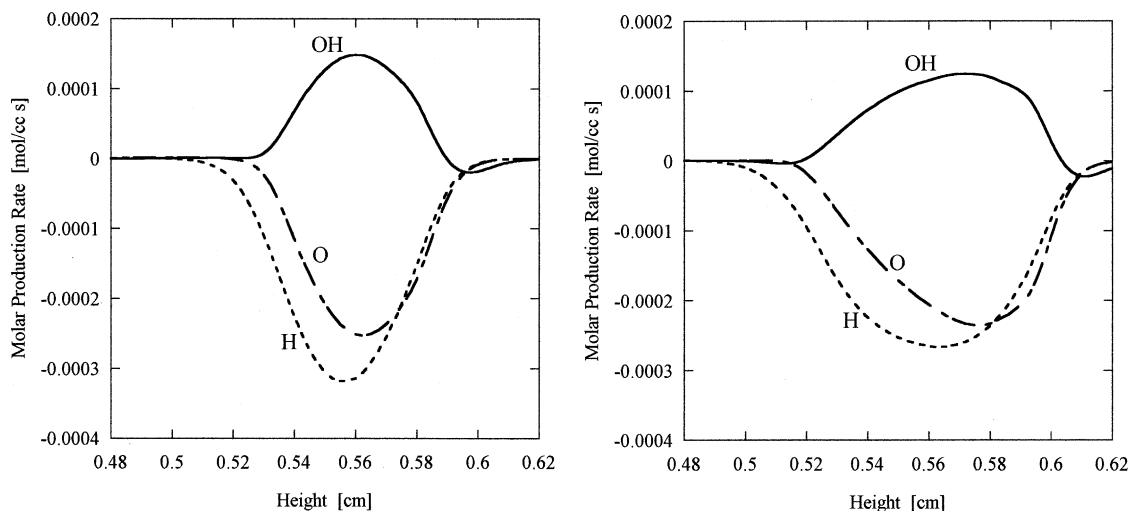


Fig. 10. a) OH, H, and O production rates in Flame 1: sum over all reactions involving phosphorus. Solid line is OH production rate, dotted line is H production rate, dot-dash line is O production rate. b) OH, H, and O production rates in Flame 4: sum over all reactions involving phosphorus. Solid line is OH production rate, dotted line is H production rate, dot-dash line is O production rate.

though the temperature dependence of the computational results is weaker. The magnitude of effectiveness from the flame calculations agrees well with LIF data from the highest temperature case, flame 4, but the calculations under-predict effectiveness for flames 1 through 3. In these calculations the magnitude of the reduction in OH (i.e., total $\text{OH}_{\text{undoped}}$ - total OH_{doped}) is nearly constant for all flames. For these flame calculations, changes in the effectiveness (which is a fractional measure of the reduction of total OH) with temperature are due mainly to the increases in the total $\text{OH}_{\text{undoped}}$, which is larger by a factor of 2.25 for flame 4 ($\text{CH}_4/\text{O}_2/\text{Ar}$) compared to flame 1 ($\text{CH}_4/\text{O}_2/\text{N}_2$) in the calculations. This estimate of the increase of total OH for the undoped flames is not sufficient to explain the variation in effectiveness observed in the LIF measurements (reduced by a factor of 10 in flame 4 compared to flame 1).

The processes responsible for the observed reductions in [OH] were determined by analysis of individual reaction rates from the phosphorus mechanism. Since the experimental and computational results both show a reduction in OH concentration with the addition of DMMP, it would be expected that the reactions involving phosphorus remove OH from the flame. In fact, for all four flames the sum of the chemical

production rates for OH over all reactions involving phosphorus in the mechanism is positive across most of the OH profile, indicating that these reactions directly produce OH rather than destroy it. Thus the drop in OH upon introduction of phosphorus kinetic sub-mechanism must occur indirectly, through an effect on rates of reactions not involving phosphorus-containing species. Poor efficiency for direct recombination of OH by reactions involving suppressant species has been observed previously for iron-based [52] and halogen-based [53, 54] suppressants. The net production rates for flame radicals OH, H, and O by all reactions involving phosphorus in flames 1 and 4 are shown in Figs. 10a and 10b, respectively. It is clear from these figures that the action of the phosphorus-containing species is similar in both flames. The regions of radical production/destruction in flame 4 are somewhat wider, in keeping with the wider flame (see Fig. 4), but the peak magnitudes of the production rates for H, O, and OH are 5 to 10% lower.

The cause of the observed reduction in OH is the fast removal of H and O atoms by the reactions involving phosphorus. Smyth et al. [55] have studied the interrelationships of H, O, and OH concentrations in non-premixed methane-air flames and found that while these species are generally not in equilibrium, their re-

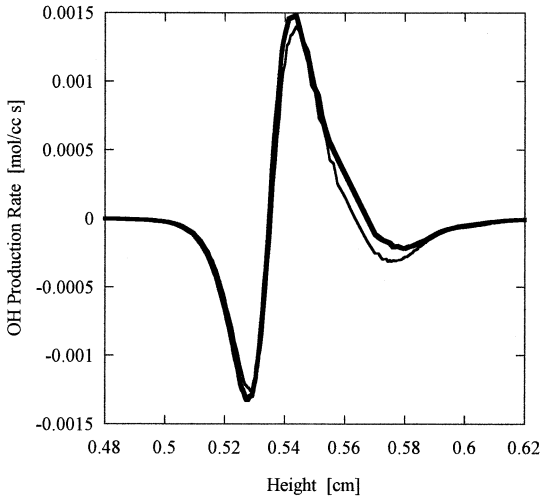


Fig. 11. Total OH production rates in flame 1 by reactions not involving phosphorus. The dark line is the undoped rate. The thin line is the rate with the addition of 572 ppm of DMMP.

spective populations are still interdependent on one another through a variety of fast radical shuffle reactions. Because of this interdependence, the reductions in H and O atom levels created by the reactions involving phosphorus, observed in Fig. 8 for flame 1, cause the radical shuffle reactions not involving phosphorus to respond by reducing OH.

Figure 11 illustrates the shift in OH production rates by the GRI sub-mechanism (sum of OH production rates over reactions not involving phosphorus) because of the addition of 572 ppm of DMMP to flame 1. The OH production in the doped flame is generally lower than that in the undoped case, particularly on the oxidizer side of the flame. The individual reactions that are primarily responsible for the shift seen in Fig. 11 were identified by comparing the shift in doped and undoped reaction rates for all reactions not involving phosphorus. Three reactions show significant shifts in OH production rates due to the presence of phosphorus. Two of these reactions, R1 and R2, undergo a substantial decrease in OH production for the doped flame. R1 is one of the important chain branching reactions:

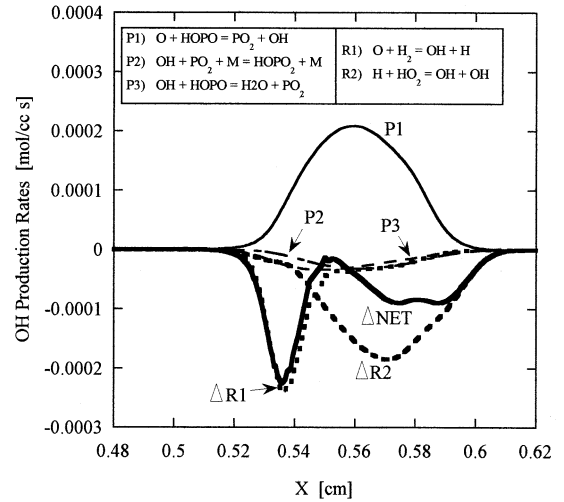
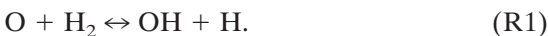


Fig. 12. Influence of the addition of 572 ppm of DMMP on OH production rates in flame 1 ($\text{CH}_4/\text{O}_2/\text{N}_2$). Rates of OH production by reactions involving phosphorus P1–P3 and changes (ΔR1 and ΔR2) in OH production (doped rate – undoped rate) for non-phosphorus containing reactions R1 and R2. The net effect (ΔNET) of these reactions is shown in bold.

The third reaction that undergoes significant changes because of addition of phosphorus is R3:



This reaction has been identified by Twarowski [3, 42, 43] as playing an important role in increased recombination rates $\text{OH} + \text{H} \rightarrow \text{H}_2\text{O}$ due to the presence of phosphorus containing compounds. In our non-premixed flames the overall effect of R3 in the presence of phosphorus addition is not clear, as the reaction has regions of increased OH production as well as regions of decreased OH production across the flame width.

Figure 12 shows the contribution of individual reactions involving phosphorus to OH production rates and compares them to the changes in the reaction rates of R1 and R2 (doped rate – undoped rate) that occur when DMMP is added to the flame 1. OH production by reactions involving phosphorus is dominated by P1:



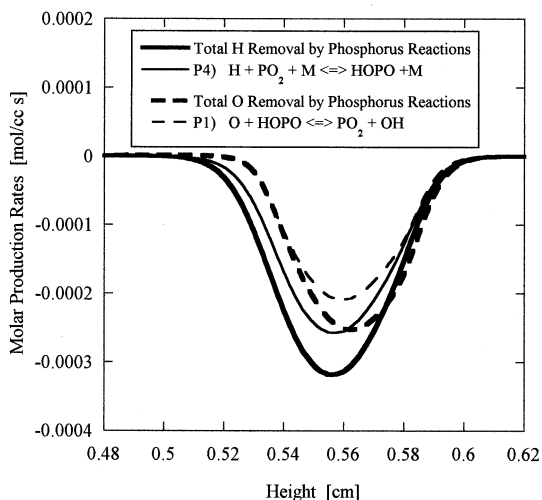


Fig. 13. H and O production rates by all reactions involving phosphorus (solid lines) and by individual reactions (dashed lines, see legend), in Flame 1.

There are two phosphorus containing reactions that consume OH, but the rates are small (15–30%) relative to P1:



Figure 12 also shows the net change in OH production for all reactions in that figure (P1, P2, P3, R1, and R2). The net rate curve shows overall destruction of OH, indicating that the shift towards decreased production by R1 and R2 is more than sufficient to balance the direct production of OH by P1.

Removal of H and O atoms by reactions involving phosphorus clearly plays an important role in the observed inhibition. Calculation results show that removal of H atoms by reactions involving phosphorus is done primarily by:



and to a lesser extent by:



Figure 13 shows the contribution of P4 to the total H destruction rate by all reactions involving phosphorus. Removal of O atoms by reactions involving phosphorus is done primarily by the OH-producing reaction P1. The contribu-

tion of P1 to O removal is also shown in Fig. 12. Significant uncertainties remain for the rate coefficients of several of the key reactions involving phosphorus species that have been identified here (P1, P2, and P4) [46]. Suggestions that the rate coefficients for the recombination reactions P2 and P4 might need to be increased by a factor of 2 or more [46] could help reconcile the observed differences in magnitude of effectiveness between the measurements and the computational predictions.

SUMMARY AND CONCLUSIONS

For the first time, quenching-corrected LIF measurements of the influence of DMMP, a phosphorus-based flame suppressant, on relative OH radical concentration profiles in moderately strained (global strain rate of 300 s^{-1}) non-premixed flames have been made. Measurement results in an atmospheric-pressure methane-air flame indicated that a loading of only 572 ppm reduces the total OH population (integrated across the flame width) by 23%. OH profiles in doped flames are smaller in magnitude than the undoped cases. As the flame temperature is increased via substitution of Ar for N_2 in the oxidizer stream, the effectiveness of DMMP is dramatically reduced. For an increase in stoichiometric adiabatic flame temperature of 300 K (all N_2 in the oxidizer stream replaced with Ar), the effectiveness of DMMP decreases by nearly 90%. The trend of increasing effectiveness at lower temperatures implies that a mixture of inert and phosphorus-based suppressants could interact synergistically as the physical agent cools the flame, thus increasing the efficiency of the chemically active component.

Calculations performed with a proposed mechanism for DMMP decomposition and phosphorus radical chemistry show reasonable agreement with the measured DMMP effectiveness and the observed temperature dependence. Measurements show a generally higher effectiveness, and a larger variation in effectiveness with temperature than that predicted by the computations with this kinetic mechanism. Significant uncertainties remain for several of the reaction rate coefficients in the phosphorus

mechanism. Further refinement of these values is still needed to improve the agreement of the computational predictions with the experimentally observed magnitude and temperature dependence of OH reductions. Analysis of the mechanism shows that the direct role of the phosphorus-containing species in the flame is the production of OH and the fast removal of H and O atoms. This removal of H and O atoms leads indirectly to the net observed decrease in OH. Calculation results show that inhibition is due to the phosphorus-containing radicals, PO₂, HOPO, and HOPO₂, formed after the decomposition of the parent compound. This result implies that flame inhibition does not depend on the form of the parent compound, provided that the parent breaks down in the flame. Thus, a broad class of potential PCC fire suppressants should exist, from which an alternative to halons with minimal health and environmental impact may be selected.

The authors gratefully acknowledge the pre-publication use of the kinetic mechanism developed by V. Babushok of NIST, and thank J. Fleming and B. Williams of the Naval Research Laboratory for their assistance and many helpful discussions. This research is part of the Dept. of Defense's Next Generation Fire Suppression Technology Program, funded by Dept. of Defense Strategic Environmental Research and Development Program under DARPA contract #MDA972-97-M-0013. Support was also provided by the Natural Sciences and Engineering Research Council of Canada.

REFERENCES

- MacDonald, M. A., Jayaweera, T. M., Fisher, E. M., and Gouldin, F. C., *Combust. Flame* 116:166–176 (1999).
- Hastie, J. W., and Bonnell, D. W., *Molecular Chemistry of Inhibited Combustion Systems*, National Bureau of Standards, Final NBSIR 80-2169; PB81-170375, 1980.
- Twarowski, A., *Combust. Flame* 94:91–107 (1993).
- Korobeinichev, O. P., Il'in, S. B., and Mokrushin, V. V., *Combust. Sci. Technol.* 116–117:51–67 (1996).
- Babushok, V., and Tsang, W., *Influence of Phosphorus-Containing Fire Suppressants on Flame Propagation*, Proc. Third Int. Conf. on Fire Res. and Eng., Chicago, IL, p. 257–267 (1999).
- Babushok, V., Tsang, W., Linteris, G. T., and Reinelt, D., *Combust. Flame* 115:551–560 (1998).
- Ibricu, M. M., and Gaydon, A. G., *Combust. Flame* 8:51–62 (1964).
- Skaggs, R. R., Daniel, R. G., Miziolek, A. W., and McNesby, K., *Spectroscopic Studies of Inhibited Opposed Flow Propane/Air Flames*, Presented at First Joint States Meeting of the U.S. Sections of the Combustion Institute, Washington, DC, 1999.
- MacDonald, M. A., Jayaweera, T. M., Fisher, E. M., and Gouldin, F. C., *Proc. Combust. Inst.* 27:2749–2756 (1998).
- Saso, Y., Ogawa, Y., Saito, N., and Wang, H., *Combust. Flame* 118:489–499 (1999).
- Lott, J. L., Christian, S. D., Sliepcevich, C. M., and Tucker, E. E., *Fire Technol.* 32:260–271 (1996).
- Reinelt, D., and Linteris, G. T., *Proc. Combust. Inst.* 26:1421–1428 (1996).
- Rumminger, M. D., and Linteris, G. T., *Combust. Flame* 120:451–464 (2000).
- Brown, T. M., Tanoff, M. A., Osborne, R. J., Pitz, R. W., and Smooke, M. D., *Combust. Sci. Technol.* 129:71–88 (1997).
- Arnold, A., Becker, H., Hemberger, R., Hentschel, W., Ketterle, W., Kollner, M., Meienburg, W., Monkhouse, P., Neckel, H., Schafer, M., Schindler, K. P., Sick, V., Suntz, R., and Wolfrum, J., *Appl. Optics* 29:4860–4872 (1990).
- Wainner, R. T., McNesby, K. L., Daniel, R. G., Miziolek, A. W., and Babushok, V. I., *Experimental and Mechanistic Investigation of Opposed-Flow Propane/Air Flames by Phosphorus-Containing Compounds*, Proc. of the 10th Halon Options Technical Working Conf., Albuquerque, NM, 2000.
- Barlow, R. S., and Collignon, A., *Linear LIF Measurements of OH in Nonpremixed Methane-Air Flames: When are Quenching Corrections Unnecessary*, AIAA 91-0179, 29th Aerospace Sciences Meeting, Reno, 1991.
- Masri, A. R., Dally, B. B., Barlow, R. S., and Carter, C. D., *Combust. Sci. Technol.* 113–114:17–34 (1996).
- Smyth, K. C., and Everest, D. A., *Proc. Combust. Inst.* 26:1385–1394 (1996).
- L'Espérance, D., Williams, B. A., and Fleming, J. W., *Combust. Flame* 117:709–731 (1999).
- Seshadri, K., and Williams, F., *Int. J. Heat Mass Transfer* 21:251–253 (1978).
- Kee, R. J., Rupley, F. M., Miller, J. A., Coltrin, M. E., Grcar, J. F., Meeks, E., Moffat, H. K., Lutz, A. E., Dixon-Lewis, G., Smooke, M. D., Warnatz, J., Evans, G. H., Larson, R. S., Mitchell, R. E., Petzold, L. R., Reynolds, W. C., Caracotsios, M., Stewart, W. E., and Glarborg, P., *Chemkin Collection, Release 3.5*, Reaction Design, Inc., San Diego, CA (1999).
- Smith, G. P., Golden, D. M., Frenklach, M., Moriarty, N. W., Eiteneer, B., Goldenberg, M., Bowman, C. T., Hanson, R. K., Song, S., Gardiner, W. C. Jr., Lissianski, V. V., and Qin, Z., GRI Mech 3.0 (1999) http://www.me.berkeley.edu/gri_mech/.
- Chelliah, H. K., Law, C. K., Ueda, T., Smooke, M. D., and Williams, F. A., *Proc. Combust. Inst.* 23:503–510 (1990).

25. Sung, C. J., Liu, J. B., and Law, C. K., *Combust. Flame* 102:481–492 (1995).
26. Ravikrishna, R. V., and Laurendeau, N. M., *Combust. Flame* 120:372–382 (2000).
27. Magre, P., Aguerre, F., Collin, G., Versaevel, P., Lacas, F., and Rolon, J. C., *Exp. Fluids* 18:376–382 (1995).
28. Beaud, P., Radi, P. P., Franzke, D., Frey, H.-M., Mischler, B., Tzannis, A.-P., and Gerber, T., *Appl. Opt.* 37:3354–3367 (1998).
29. Smith, G. P., and Crosley, D. R., *Appl. Opt.* 22:1428–1430 (1983).
30. Allen, M. G., McManus, K. R., Sonnenfroh, D. M., and Paul, P., *Appl. Opt.* 34:6287–6300 (1995).
31. Puri, R., Moser, M., Santoro, R. J., and Smyth, K. C., *Proc. Combust. Inst.* 24:1015–1022 (1992).
32. Arnold, A., Bombach, R., Käppeli, B., and Schlegel, A., *Appl. Phys. B—Lasers Opt.* 64:579–583 (1997).
33. Kelman, J. B., and Masri, A. R., *Appl. Optics* 33:3992–3999 (1994).
34. Köllner, M., and Monkhouse, P., *Appl. Phys. B* 61:499–503 (1995).
35. Norton, T. S., Smyth, K. C., Miller, J. H., and Smooke, M. D., *Combust. Sci. Technol.* 90:1–34 (1993).
36. Crosley, D. R., *High Temp. Material Proc.* 7:41–54 (1986).
37. Luque, J., and Crosley, D. R., *LIFBASE: Database and Simulation Program (v 1.6)*, SRI International Report MP 99-009 (1999).
38. Paul, P. H., *J. Quant. Spectrosc. Radiat. Transfer* 51: 511–524 (1994).
39. Paul, P., *J. Phys. Chem.* 99:8472–8476 (1995).
40. Hartlieb, A. T., Markus, D., Kreutner, W., and Kohse-Höinghaus, K., *Appl. Phys. B* 65:81–91 (1997).
41. Tamura, M., Berg, P. A., Harrington, J. E., Luque, J., Jefferies, J., Smith, G. P., and Crosley, D. R., *Combust. Flame* 114:504–514 (1998).
42. Twarowski, A., *Combust. Flame* 102:55–63 (1995).
43. Twarowski, A., *Combust. Flame* 102:41–54 (1995).
44. Werner, J. H., and Cool, T. A., *Combust. Flame* 117:78–98 (1999).
45. Mokrushin, V. V., Bol'shova, T. A., and Korobeinichev, O. P., *A Kinetic Model for the Destruction of TMP in a Hydrogen/Oxygen Flame*, unpublished.
46. Babushok, V. I., personal communication, 2000.
47. Mallard, W. G., and Linstrom, P. J., Eds., *NIST Chemistry Webbook*, NIST Standard Ref. Database 69, 1998.
48. Gurvich, L. V., and Glushkov, V. P., *Thermodynamic Properties of Individual Substances*, NIST Special Database 5, IVANTHERMO-PC, 1998.
49. Melius, C., http://hertzberg.ca.sandia.gov/carl_melius.html, 1998.
50. Fisher, E. M., Williams, B. A., and Fleming, J. W., *Determination of the Strain in Counterflow Diffusion Flames from Flow Conditions*, Presented at Fall Technical Meeting of the Combustion Institute, Eastern States Section, Hartford, CT, 1997.
51. MacDonald, M. A., *Ph.D. Dissertation*, Cornell University, (2000).
52. Rumminger, M. D., Reinelt, D., Babushok, V. I., and Linteris, G. T., *Combust. Flame* 116:207–219 (1999).
53. Linteris, G. T., and Truett, L., *Combust. Flame* 105: 15–27 (1996).
54. Hynes, R. G., Mackie, J. C., and Masri, A. R., *Combust. Flame* 113:554–565 (1998).
55. Smyth, K. C., Tjossem, P. J. H., Hamins, A., and Miller, J. H., *Combust. Flame* 79:366–380 (1990).

Received 5 June 2000; revised 2 October 2000; accepted 30 October 2000